Near-field spectroscopic properties of complementary gold nanostructures: applicability of Babinet's principle in the optical region

HIDETOSHI MIZOBATA,[1] KOSEI UENO,[2] HIROAKI MISAWA,[2,3] HIROMI OKAMOTO,[4] AND KOHEI IMURA[1,*]

[1]*Faculty of Science and Engineering, Waseda University, Shinjuku, Tokyo 169-8555, Japan*
[2]*Research Institute for Electronic Science, Hokkaido University, Kitaku, Sapporo, Hokkaido 001-0021, Japan*
[3]*Department of Applied Chemistry & Institute of Molecular Science, National Chiao Tung University, Hsinchu 30010, Taiwan*
[4]*Institute for Molecular Science and The Graduate University for Advanced Studies (Sokendai), Myodaiji, Okazaki, Aichi 444-8585, Japan*
[*]*imura@waseda.jp*

Abstract: We examine the far-field and near-field properties of complementary screens made of nanostructured gold thin films, a rectangular nanowire and a nanovoid, using an aperture-type scanning near-field optical microscope and electromagnetic field calculations, and discuss the applicability of Babinet's principle in the optical region. The far-field transmission spectra of the complementary screens are considerably different from each other. On the other hand, genuine near-field extinction spectra exhibit nearly complementary characteristics. The spatial features of the observed near-field images for the complementary screens show little correlation. We have found from the Fourier analysis of the simulated images that high spatial-frequency components of the electromagnetic fields show mutual spatial correlation. These results suggest that Babinet's principle is applicable to the high spatial-frequency components of electromagnetic fields for the complementary screens.

References and links

1. C. Vieu, F. Carcenac, A. Pepin, Y. Chen, M. Mejias, A. Lebib, L. Manin-Ferlazzo, L. Couraud, and H. Launois, "Electron beam lithography: resolution limits and applications," Appl. Surf. Sci. **164**(1-4), 111–117 (2000).
2. S. A. Maier, *Plasmonics: fundamentals and applications* (Springer, 2007).
3. R. M. Ma, R. F. Oulton, V. J. Sorger, and X. Zhang, "Plasmon lasers: coherent light source at molecular scales," Laser Photonics Rev. **7**(1), 1–21 (2013).
4. J. Chen, Z. Li, X. Zhang, J. Xiao, and Q. Gong, "Submicron bidirectional all-optical plasmonic switches," Sci. Rep. **3**, 1451 (2013).
5. X. Yang, X. Hu, H. Yang, and Q. Gong, "Ultracompact all-optical logic gates based on nonlinear plasmonic nanocavities," Nanophotonics **6**(1), 365–376 (2017).
6. V. G. Veselago, "The electrodynamics of substances with simultaneously negative values of ε and μ," Sov. Phys. Usp. **10**(4), 509–514 (1968).
7. D. R. Smith, W. J. Padilla, D. C. Vier, S. C. Nemat-Nasser, and S. Schultz, "Composite medium with simultaneously negative permeability and permittivity," Phys. Rev. Lett. **84**(18), 4184–4187 (2000).
8. R. A. Shelby, D. R. Smith, and S. Schultz, "Experimental verification of a negative index of refraction," Science **292**(5514), 77–79 (2001).
9. S. A. Ramakrishna, "Physics of negative refractive index materials," Rep. Prog. Phys. **68**(2), 449–521 (2005).
10. J. B. Pendry, "Negative refraction makes a perfect lens," Phys. Rev. Lett. **85**(18), 3966–3969 (2000).
11. N. Fang, H. Lee, C. Sun, and X. Zhang, "Sub-diffraction-limited optical imaging with a silver superlens," Science **308**(5721), 534–537 (2005).
12. Z. Liu, H. Lee, Y. Xiong, C. Sun, and X. Zhang, "Far-field optical hyperlens magnifying sub-diffraction-limited objects," Science **315**(5819), 1686 (2007).

13. J. B. Pendry, D. Schurig, and D. R. Smith, "Controlling electromagnetic fields," Science **312**(5781), 1780–1782 (2006).
14. U. Leonhardt, "Optical conformal mapping," Science **312**(5781), 1777–1780 (2006).
15. D. Schurig, J. J. Mock, B. J. Justice, S. A. Cummer, J. B. Pendry, A. F. Starr, and D. R. Smith, "Metamaterial electromagnetic cloak at microwave frequencies," Science **314**(5801), 977–980 (2006).
16. H. G. Booker, "Slot aerials and their relation to complementary wire aerials," J. Inst. Electr. Eng. **93**(4), 620–626 (1946).
17. M. Born and E. Wolf, *Principles of Optics 7th ed.* (Cambridge University, 1999), Chap. 11.
18. J. D. Jackson, *Classical Electrodynamics 3rd ed.* (Wiley & Sons, 1999), Chap.10.
19. F. Falcone, T. Lopetegi, M. A. A. Laso, J. D. Baena, J. Bonache, M. Beruete, R. Marqués, F. Martín, and M. Sorolla, "Babinet principle applied to the design of metasurfaces and metamaterials," Phys. Rev. Lett. **93**(19), 197401 (2004).
20. T. Zentgraf, T. P. Meyrath, A. Seidel, S. Kaiser, H. Giessen, C. Rockstuhl, and F. Lederer, "Babinet's principle for optical frequency metamaterials and nanoantennas," Phys. Rev. B **76**(3), 033407 (2007).
21. N. Liu, S. Kaiser, and H. Giessen, "Magnetoinductive and electroinductive coupling in plasmonic metamaterial molecules," Adv. Mater. **20**(23), 4521–4525 (2008).
22. A. Bitzer, A. Ortner, H. Merbold, T. Feurer, and M. Walther, "Terahertz near-field microscopy of complementary planar metamaterials: Babinet's principle," Opt. Express **19**(3), 2537–2545 (2011).
23. B. T. Draine and P. J. Flatau, "User guide for the discrete dipole approximation code DDSCAT 7.3," http://arxiv.org/abs/1305.6497.
24. E. M. Purcell and C. R. Pennypacker, "Scattering and absorption of light by nonspherical dielectric grains," Astrophys. J. **186**, 705–714 (1973).
25. B. T. Draine, "The discrete-dipole approximation and its application to interstellar graphite grains," Astrophys. J. **333**, 848–872 (1988).
26. J. J. Goodman, P. J. Flatau, and B. T. Draine, "Application of fast-Fourier-transform techniques to the discrete-dipole approximation," Opt. Lett. **16**(15), 1198–1200 (1991).
27. B. T. Draine and P. J. Flatau, "Discrete-dipole approximation for scattering calculations," J. Opt. Soc. Am. A **11**(4), 1491–1499 (1994).
28. B. T. Draine and P. J. Flatau, "Discrete-dipole approximation for periodic targets: theory and tests," J. Opt. Soc. Am. A **25**(11), 2693–2703 (2008).
29. P. J. Flatau and B. T. Draine, "Fast near field calculations in the discrete dipole approximation for regular rectilinear grids," Opt. Express **20**(2), 1247–1252 (2012).
30. P. B. Johnson and R. W. Christy, "Optical constants of the noble metals," Phys. Rev. B **6**(12), 4370–4379 (1972).
31. K. Imura, T. Nagahara, and H. Okamoto, "Characteristic near-field spectra of single gold nanoparticles," Chem. Phys. Lett. **400**(4–6), 500–505 (2004).
32. K. Imura, K. Ueno, H. Misawa, and H. Okamoto, "Anomalous light transmission from plasmonic-capped nanoapertures," Nano Lett. **11**(3), 960–965 (2011).
33. B. J. Messinger, U. K. von Raben, R. K. Chang, and P. W. Barber, "Local fields at the surface of noble-metal microspheres," Phys. Rev. B **24**(2), 649–657 (1981).
34. K. Imura, T. Nagahara, and H. Okamoto, "Near-field optical imaging of plasmon modes in gold nanorods," J. Chem. Phys. **122**(15), 154701 (2005).
35. H. Okamoto and K. Imura, "Near-field optical imaging of enhanced electric fields and plasmon waves in metal nanostructures," Prog. Surf. Sci. **84**(7–8), 199–229 (2009).
36. K. L. Kelly, E. Coronado, L. L. Zhao, and G. C. Schatz, "The optical properties of metal nanoparticles: the influence of size, shape, and environment," J. Phys. Chem. B **107**(3), 668–677 (2003).
37. A. Brioude and M. P. Pileni, "Silver nanodisks: optical properties study using the discrete dipole approximation method," J. Phys. Chem. B **109**(49), 23371–23377 (2005).

1. Introduction

Recent advances in fabrication technique allow to design nanostructures of various substances with a nanometer scale [1]. Optical and electrical properties of the nanomaterials have been extensively studied because of their fundamental importance and potential applications in applied optics [2]. For example, metal nanostructures have been utilized for developing nanoscale optical devices such as a nansclae laser [3], ultrafast switches [4], logic circuits [5], and so on. A deep understanding of the optical properties of nanomaterials is a prerequisite for the development of novel optical materials. One of the typical examples is the development of metamaterials. Based on the striking characteristics of negative refractive indices, the applications of metamaterials to unique optical devices such as super lenses are discussed [6–15]. They are usually composed of periodic arrays of subwavelength structures, called building units. The optical properties of metamaterials depend on the geometrical structures and dielectric properties of the building units. In the design of the building units,

Babinet's principle, which discusses the optical properties of a pair of geometrically complementary screens made of conducting materials [16–18], is sometimes utilized as a guiding principle. Suppose that the electric and magnetic fields incident on an opaque conducting screen are $\mathbf{E}_0$ and $\mathbf{B}_0$, respectively, and those on its complementary screen are $\mathbf{E}_0^c$ and, $c\mathbf{B}_0^c$ respectively. Babinet's principle states that, when two screens are illuminated with complementary waves expressed by

$$\mathbf{E}_0^c = -c\mathbf{B}_0 \quad \text{and} \quad c\mathbf{B}_0^c = \mathbf{E}_0 \tag{1}$$

the diffracted electric and magnetic fields from the screen ($\mathbf{E}$, $\mathbf{B}$) and those from the complementary screen ($\mathbf{E}^C$, $\mathbf{B}^C$) satisfy the relation

$$c\mathbf{B}^c + \mathbf{E} = c\mathbf{B}_0^c \tag{2}$$

$$\mathbf{E}^c - c\mathbf{B} = \mathbf{E}_0^c \tag{3}$$

where c is the speed of light. Equations (2) and (3) indicate that the spatial distribution of the electric field diffracted by the screen, $\mathbf{E}$, should be identical to that of the magnetic field diffracted by the complementary counterpart, $\mathbf{B}^C$, and *vice versa*. Babinet's principle also states that the transmittance of the screen (T) is connected with that of the complementary counterpart (T^C) by the following equation:

$$T + T^C = 1 \tag{4}$$

Equation (4) indicates that transmittance of the screen shows an inverted spectral response compared with that of the complementary counterpart, *i.e.,* positive peaks in a transmission spectrum of the screen should appear as negatives peaks in that of the complementary screen.

In Babinet's principle, the screens are assumed to be infinitely thin and made of perfect conductors. In the long wavelength regions, such as the microwave and terahertz wave regions, these requirements are satisfied sufficiently well, and thus, the optical properties of a screen are predictable from those of the complementary screen using this principle [19–22]. In the optical region, however, the above prerequisites are no longer valid because the practically available metals, such as gold and silver, which are often used for metamaterials, show interband transitions that make them non-perfect conductors. In addition, the thickness of the available screens, generally thicker than a few tens of nanometers, is not thin enough to be regarded as infinitely thin compared to the wavelength of visible light. Therefore, it is not straightforward to apply Babinet's principle to such real screens in the optical region. We should clarify the applicability and limitation of this principle in detail, because the principle gives us useful guidelines for designing not only the metamaterials but also the novel optical devices such as ultra-small sensors, highly efficient solar cells, and so forth. In this study, we investigated the far- and near-field optical properties of complementary gold nanostructures, a gold rectangular nanowire and its complementary nanovoid on a thin gold film, and discussed the applicability of Babinet's principle in the optical region.

2. Sample preparations and experimental apparatus

We fabricated gold nanowires and nanovoids on a cover slip using the electron beam lithography and lift-off techniques. Sample substrate was then spin-coated by a polyvinyl alcohol (PVA) thin film (~10 nm) to homogenize refractive index of the medium surrounding the gold nanostructures. The far- and near-field optical properties of the samples were examined using a homemade aperture-type scanning near-field optical microscope (SNOM). A schematic diagram of the apparatus is depicted in Fig. 1, together with a scanning electron micrograph image of a gold-coated near-field fiber probe (JASCO). The SNOM was operated in the illumination mode. The sample was illuminated through an aperture of the near-field

fiber probe. The transmitted light from the sample was collected with a high numerical aperture objective lens and detected by a charge-coupled device (CCD, Andor DU920P-OE) equipped with a polychromator. A xenon discharge lamp was used as a white light source. The diameter of the aperture of the near-field probe was 50–100 nm. A linear polarizer was installed before the polychromator in order to probe the polarization characteristics of the samples. A sample substrate was mounted on a piezo-driven stage (PI, P-733.3CD). For near-field transmission measurements, the distance between the near-field probe tip and the sample surface was kept constant at ~10 nm using a shear-force feedback mechanism. For far-field transmission measurements, the distance was adjusted to ~1 μm.

To analyze the optical characteristics of the samples in detail, we also performed electromagnetic calculations using a discrete dipole approximation (DDA) method [23–29]. The dimensions of the nanostructured samples used for the calculations were identical to those of the fabricated ones. For calculations of the nanovoid, the periodic boundary condition was adopted, with a unit cell of 3 μm × 3 μm in the direction of the sample surface, to reduce the scattering signals from the edges of samples. The spacing between the point dipoles was set to be 2.5 nm for the calculations. The incident light was a plane wave with a linear polarization and impinged normal to the sample surface. The dielectric function of gold was adopted from the literature [30]. The refractive index of the surrounding medium was 1.5.
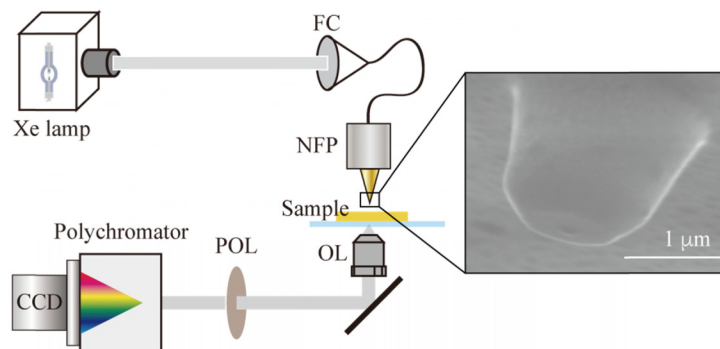

Fig. 1. A schematic diagram of a homemade aperture-type SNOM. FC: fiber coupler, NFP: aperture near-field probe, OL: objective lens, POL: polarizer, CCD: charge-coupled device detector. Inset: scanning electron micrograph of a gold-coated NFP tip.

3. Results and discussions

Figure 2 shows scanning electron micrographic images of the fabricated single gold nanowire and nanovoid. The dimensions of each nanostructure were determined to be 690 ± 10 nm in length, 90 ± 5 nm in width, and 20 ± 0.5 nm in height. The dimensions of the nanowire were identical to those of the nanovoid within an accuracy of 10 nm.
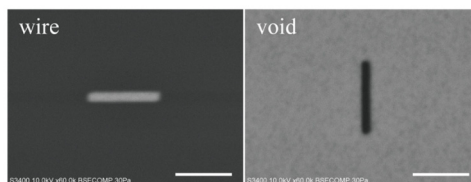

Fig. 2. Scanning electron micrographs of a fabricated single gold nanowire (left) and nanovoid (right). Scale bar is 500 nm. The dimensions of the nanostructures are 690 ± 10 nm in length, 90 ± 5 nm in width, and 20 ± 0.5 nm in height
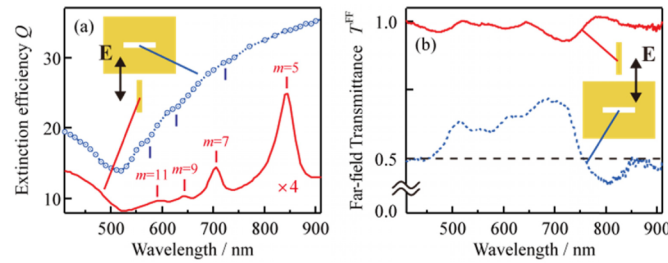
3.1 Far-field spectroscopic properties

Fig. 3. (a) Simulated polarized extinction Q and (b) polarized transmission spectra T^{FF} of a single gold nanowire (solid red curve) and nanovoid (dotted blue curve) obtained under the far-field illumination. Schematic illustrations indicate the orientation of the samples relative to the detected polarization. Bars in (a) indicate the location of the resonance.

We calculated far-field spectral characteristics of the gold wire and the nanovoid using the DDA method. Figure 3(a) shows the simulated extinction spectra of the wire (solid red line) and the nanovoid (dotted blue line). In the extinction spectrum of the nanowire, multiple peaks are observed at 590, 640, 700, and 840 nm. These peaks are assigned to longitudinal plasmon resonances, based on their polarization and spatial characteristics. Plasmon mode index (m) is provided near the peaks in Fig. 3(a). In the extinction spectrum of the nanovoid, a broad dip near 520 nm and a monotonous increase in the long wavelength region were observed. The spectral profile is very similar to that of the gold thin film. Optical features are dominated by the gold thin film because in the simulation the plane wave is used for illumination and thus illumination area for the film is much larger than that for the nanovoid. Consequently, optical properties due to a small structure is smeared out by those due to the large one. A close inspection of the spectrum, however, a few tiny dips near 580 nm, 620 nm, and 720 nm are barely visible.

Figure 3(b) shows polarized transmission spectra of the single gold nanowire and the nanovoid taken under far-field illumination. The solid (red) and dotted (blue) curves represent the transmission spectra for the nanowire and the nanovoid, respectively. The transmittance T_{FF} ($= I_{sample} / I_{substrate}$) was obtained from transmission intensity obtained at the sample (I_{sample}) and at the bare substrate ($I_{substrate}$). Illumination spot size was limited to ca. 1-2 μm for effectively observing optical properties of the structures. The schematic illustrations in the figure show the orientations of the samples relative to the polarization (electric field) directions detected. The polarization directions are compatible with the conditions required for the application of Babinet's principle as described in Eq. (1). Since the magnitude of the transmittance depends on area of the illumination, we mainly discuss the observed spectral profiles. In the transmission spectrum of the nanowire, negative peaks are observed at 550, 600, 720 nm, and ca. 830 nm. Peak positions in the simulated spectrum, except for a peak near 640 nm, shows qualitative agreement with those of the observed ones, and therefore the observed peaks are assigned to the plasmon resonances. A peak near 640 nm in Fig. 3(b) is not visible because of the spectral overlap with the nearby peaks. In the transmission spectrum of the nanovoid, positive peaks are observed at 550, 610, 710 nm, and 850 nm. These resonances matches qualitatively with the simulated ones, and thus observed peaks are assignable to the plasmon resonances excited in the nanovoid.

Provided that Babinet's principle is applicable to the present system, the resonance wavelengths of the nanovoid should be identical to those of the nanowire and signs of the peaks in the nanovoid should be opposite compared with those in the nanowire. Thereby, a transmission spectrum of the nanovoid should be identical to the inverted spectrum of the nanowire with respect to the dashed line in Fig. 3(b). The observed transmission spectrum of the nanovoid shows resonance wavelengths close to those of the nanowire. However, the

observed spectral profile of the nanovoid deviates significantly from the inverted profile of the nanowire. The result indicates that the complementary pair of gold nanostructures does not exhibit spectral profiles expected from Babinet's principle.

3.2 Near-field spectroscopic properties

Near-field optical imaging of the nanowire and nanovoid were conducted to obtain further information on the optical characteristics of the complementary screens and to reveal the origin of the deviation from Babinet's principle. Near-field transmission spectra of the nanowire and nanovoid are shown in Fig. 4(a) as the solid (red) and dotted (blue) curves, respectively. Near-field transmittance T^{NF} ($= I/I_0$) was obtained from the transmission intensity at a glass substrate (I_0) and that at the center of the sample (I). The polarization directions for the near-field measurements were parallel to the long axis of the nanowire and perpendicular to that of the nanovoid, which are the same as those for the far-field measurements. The near-field spectra were found to be more complicated than the far-field ones. The near-field transmission spectrum of the nanowire showed negative peaks at 520, 630, 700, 740, 810, and 920 nm, while the nanovoid showed positive peaks at 550, 650, 720, 740, 840, and 920 nm. The peaks observed near 740 and 920 nm were only observable in the near-field spectrum. These peaks are also attributable to plasmon resonances excited in these nanostructures, as discussed later. Similar to the far-field transmission spectra in Fig. 3(b), the near-field transmission spectra showed spectral features that are only partially complementary to each other. To apply Babinet's principle rigorously, screens should be infinitely thin and perfect conductors, and thus, plasmon excitations should not be involved. In the present system, however, plasmon resonances are excited. This implies that plasmon excitations are partially responsible for the deviations from Babinet's principle.

It is worth noting here that a change of transmittance observed in a near-field transmission spectrum involves both evanescent (near-field) and propagating (far-field) wave components, since the near-field aperture probe provides not only near-field light but also far-field one [31, 32]. A genuine near-field extinction spectrum is therefore obtainable by subtracting the far-field extinction components from the near-field transmission spectrum. Near-field transmittance T^{NF} in Fig. 4(a) is thus given as

$$T^{\mathrm{NF}} = 1 - p Q_{\mathrm{ext}}^{\mathrm{NF}} - q Q_{\mathrm{ext}}^{\mathrm{FF}} \qquad (5)$$

where $Q_{\mathrm{ext}}^{\mathrm{NF}}$ is the near-field extinction efficiency, which is composed of the near-field scattering efficiency and the absorption [33]. $Q_{\mathrm{ext}}^{\mathrm{FF}}$ represents the far-field extinction efficiency and is expressed as $Q_{\mathrm{ext}}^{\mathrm{FF}} = 1 - T^{\mathrm{NF}}$, where T^{FF} is the far-field transmittance shown in Fig. 3, and p and q are the amplitude parameters for the near-field and far-field contributions, respectively. From Eq. (5), the genuine near-field extinction efficiency, $Q_{\mathrm{ext}}^{\mathrm{NF}}$, was determined by the following equation.

$$Q_{\mathrm{ext}}^{\mathrm{NF}} = (1 - T^{\mathrm{NF}} - q Q_{\mathrm{ext}}^{\mathrm{FF}}) / p = \left[1 - T^{\mathrm{NF}} - q(1 - T^{\mathrm{FF}}) \right] / p \qquad (6)$$

We should note here that spectral profiles of the near-field extinction depend only on the parameter q. We optimized the parameters q by balancing the amplitudes of $Q_{\mathrm{ext}}^{\mathrm{NF}}$ for the nanowire and the nanovoid. We used the same parameter for the nanowire and nanovoid in the analysis. Figure 4(b) shows the near-field extinction spectra of the nanowire and nanovoid obtained with the parameters ($p = 1.00$ and $q = 1.88$) in Eq. (6). In the near-field extinction spectrum obtained in this analysis, the positive and negative peaks correspond to reductions and enhancements of the near-field transmission intensity, respectively, compared with that observed at the substrate. In the near-infrared region, the nanowire shows positive peaks of $Q_{\mathrm{ext}}^{\mathrm{NF}}$ most likely due to reduced transmission by localized plasmon excitations, while the

nanovoid shows negative peaks due to enhanced transmission (reduced reflection) by plasmon excitations. Figure 4(c) show a sum spectrum of the near-field extinction spectra obtained for the nanowire and nanovoid. For the spectral range longer than 620 nm in Fig. 4(b), the spectral features of the nanowire are nearly identical to the inverted spectral profile of the nanovoid with respect to the zero line. As a consequence, the sum spectrum in Fig. 4(c) remains approximately null in this spectral region. The result is consistent with the spectral complementarity related to Babinet's principle. On the other hand, for the spectral wavelength range shorter than 620 nm, the spectra for the nanowire and nanovoid show little complementarity because of the interband transitions of gold.
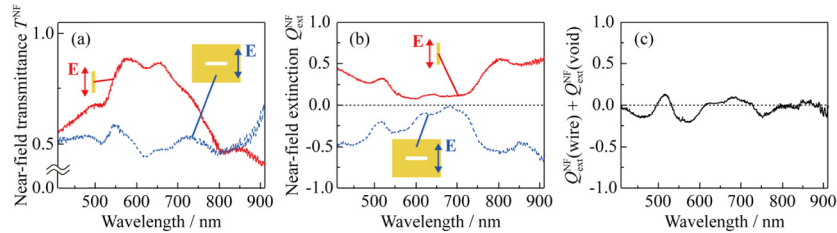

Fig. 4. (a) Near-field transmission spectra T^{NF} of a single gold nanowire (solid red curve) and nanovoid (dotted blue curve). The polarization directions were parallel to the long axis of the nanowire and perpendicular to that of the nanovoid, which were the same as those for the far-field measurements. (b) Near-field extinction spectra Q_{ext}^{NF} of a single gold nanowire (solid red curve) and nanovoid (dotted blue curve) obtained by subtracting the far-field transmission spectra from the near-field ones (for details see the text). (c) A sum spectrum of Q_{ext}^{NF} for the nanowire and nanovoid.

3.3 Near-field spatial properties

Next, we visualized a spatial distribution of the excitation probability of the samples. Figures 5(a), 5(c), and 5(e) and Figs. 5(b), 5(d), and 5(f) show near-field transmission images of the nanowire and the nanovoid, respectively. The wavelengths of observation were Figs. 5(a)–5(b) 738–748 nm, Figs. 5(c)–5(d) 812–821 nm, and Figs. 5(e)–5(f) 916–926 nm. The arrows indicate the polarization directions of the detected photons. The dark parts indicate the reduction of transmission intensity due to the absorption and scattering of light. The excitation probability in the nanowire oscillates periodically along the long axis of the nanowire. The number of dark spots decreases as the observed wavelength becomes longer. The result implies that the dark spots correspond to antinodes of the plasmonic standing waves induced in the nanowire, and thus, the oscillating features observed are attributable to the (a) 6th, (c) 5th, and (e) 4th longitudinal plasmon modes [34,35]. We should mention here that the plasmon modes with even *m* values are only accessible by the local excitation with the near-field probe. These are optically forbidden modes by a plane wave excitation, since the polarizations induced in the wire becomes null due to the symmetry of the mode. For this reason, the near-field transmission spectra show additional resonances near 740 and 920 nm with respect to the far-field ones.

In the transmission images of the nanovoid shown in Figs. 5(b), 5(d), and 5(f), the excitation probability is almost constant along the long axis of the nanovoid. On the other hand, the excitation probability on the film (outside of the void) oscillates periodically along the perpendicular direction to the long axis of the nanovoid. We obtained the dispersion relation of the oscillation by plotting the resonance energy against the wave vector. The wave vector was evaluated from the period of oscillation in the image, and the resonance energy of the oscillation mode was obtained from the near-field transmission spectrum. The dispersion relation determined in this manner agrees well with that predicted for surface plasmons on a gold film. The oscillations observed in Figs. 5(b), 5(d), and 5(f) are thus assigned to the

plasmons excited on the gold film. Origin of the oscillation pattern in Fig. 5 is explained as follows: upon the near-field excitation on the gold film, surface plasmon is excited. Then, the excited plasmon propagates on the gold film and is reflected back at the edge of the void. At the near-field excitation point, the excited and reflected plasmons interfere with each other and generate a standing wave. Amplitude of the standing wave depends on a distance between the excitation point and the edge of the void. As a consequence, the periodic oscillation was observed in the near-field images.
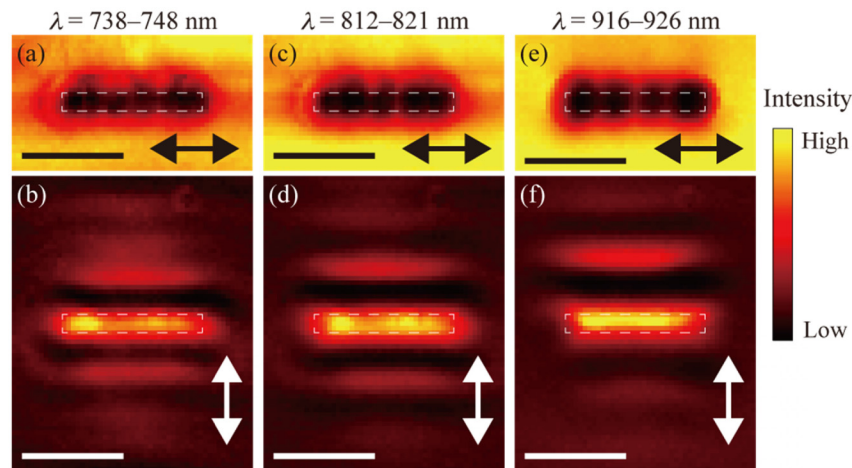

Fig. 5. Near-field transmission images of a single gold nanowire in (a), (c), and (e) and nanovoid in (b), (d), and (f). Observation wavelengths: (a) and (b) 738–748 nm, (c) and (d) 812–821 nm, (e) and (f) 916–926 nm. The arrows indicate the detected polarization directions. The white dotted lines indicate the outlines of the nanowire and nanovoid. Scale bars are 500 nm.

Now, we discuss the applicability of Babinet's principle from the viewpoint of the spatial features of the near-field transmission images. Babinet's principle states that the spatial distribution of the diffracted fields for the nanowire is identical to that for the nanovoid under the appropriate incident polarization conditions. Comparing the near-field transmission images of the nanowire and nanovoid in Fig. 5, the spatial features are found to be not identical with each other. This may indicate that the observed near-field images in Fig. 5 are not compatible with the expectation from Babinet's principle. According to the principle, the electric field diffracted by the screen should be compared with the magnetic field diffracted by the complementary counterpart. The different spatial characteristics observed for the complementary structures, therefore, should be originated from both or either the following two factors. One is that the electric field for the structure is not compared with the magnetic field for the counter one. The other one is that the prerequisite conditions for the application of the principle are not fully satisfied.

3.4 Simulated electromagnetic field distributions

To analyze the correlation between the electric and magnetic fields in the nanowire and nanovoid, we compared simulated electromagnetic field distributions for these complementary structures using DDA calculations. We discuss here the 5th longitudinal plasmon mode for the wire and the corresponding mode for the void, since the other 4th and 6th plasmon modes in Figs. 5(a) and 5(e) are dipolar forbidden and are not accessible by a plane wave excitation in the DDA calculation. Figures 6(a) and 6(b) show the electric field for the nanowire and the magnetic field for the nanovoid, respectively, simulated at 840 nm. In these images, the fields were obtained at 2.5 nm above the nanostructures. The arrows indicate the incident polarization directions. The excitation wavelength for the simulation is

slightly longer than that for the observation, because geometrical shapes of the corners for the fabricated structures were not accurately modeled with the simulation. It is known that the rounding the corner induces the blue-shift of the resonance [36,37]. For this reason, we compared the simulated results obtained at 840 nm with the observed images taken near 820 nm. The simulated image in Fig. 6(a) qualitatively reproduces the observed spatial features in Fig. 5(c). Namely, the electric field distribution for the nanowire shows a spatially oscillating feature attributable to the 5th longitudinal plasmon mode of the wire. For the nanovoid, in contrast, plasmonic standing waves are found on the gold film outside of the void, with wave vectors perpendicular to the long axis of the void. The electric field distribution for the nanowire is totally different from the magnetic field distribution for the nanovoid, as is consistent with the experimental observations. The results indicate that Babinet's principle is apparently not applicable for the prediction of the spatial characteristics of the optical field on a screen made of gold from those on a complementary counterpart in the visible and near-infrared spectral regions.
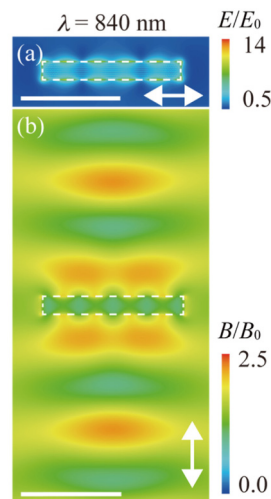

Fig. 6. Calculated electromagnetic field distributions for a gold nanowire and a nanovoid: The electric field (E) of the nanowire at 840 nm (a); the magnetic field (B) of the nanovoid at 840 nm (b). The arrows indicate the incident polarization directions. The white dotted lines indicate the outlines of the nanostructures. Scale bars are 500 nm.

Here, we should note that the near-field components of the extinction spectra in Fig. 4(b) showed consistency with Babinet's principle, which gave complementary spectra. This fact suggests that Babinet's principle is applicable to the present system as far as the near-field spectral components are concerned. Therefore, the spatial features of the optical near-fields are possibly compatible with Babinet's principle for complementary screens in a similar way as the spectral features. Near-field signals originate dominantly from higher spatial-frequency components of electromagnetic fields than far-field signals do, and thus, the high spatial-frequency components of the electromagnetic field distribution presumably give the near-field contribution. We here discuss the applicability of Babinet's principle to the spatial features of the optical near-fields by extracting the high spatial-frequency components of the electromagnetic field distributions. Fourier analyses were conducted for the electric field distribution on the nanowire in Fig. 6(a) and the magnetic field distribution on the nanovoid in Fig. 6(b). In the analysis procedure, the original electromagnetic field images were first converted into spatial-frequency images by two-dimensional Fourier transformation. The spatial-frequency components from 8 to 200 μm^{-1} were then extracted from the transformed images by a circular band-pass edge filter. Finally, the high spatial-frequency components of the electromagnetic field distributions were reconstructed by inverse Fourier transformation.

The high-frequency limit of the band-pass filter (200 μm^{-1}) was determined from a half of an inverse of the dipole size for electromagnetic calculations (2.5 nm), and the low-frequency limit (8 μm^{-1}) was set by considering the reasons described below.
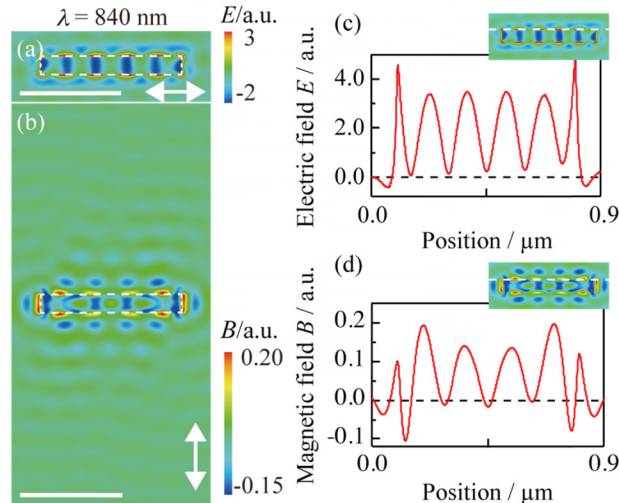

Fig. 7. The high spatial frequency components of the electromagnetic field distributions for the gold nanowire and the nanovoid based on Fourier analysis (for details see the text): The electric field (E) of the nanowire at 840 nm (a); the magnetic field (B) of the nanovoid at 840 nm (b). The spatial frequency range was from 8 μm^{-1} to 200 μm^{-1}. The arrows indicate the incident polarization directions. The white dotted lines indicate the outlines of the nanostructures. Scale bars are 500 nm. (c,d) Line profiles of the field distributions for the nanowire and nanovoid taken along the long side of the structure.

Figures 7(a) and 7(b) show the extracted high spatial-frequency components of the electric (for the nanowire) and magnetic (for the nanovoid) field distributions, respectively. The excitation wavelength was 840 nm. The spatial features for the nanowire in Fig. 7(a) are very similar to those in Fig. 6(a). On the other hand, spatial features for the nanovoid in Fig. 7(b) are markedly different from those in Fig. 6(b). Specifically, the spatially oscillating features on the metal film are significantly reduced in Fig. 7(b), compared to those in Fig. 6(b). As a consequence, spatial features in the vicinity of the void become very prominent in Fig. 7(b). The spatial variation observed from Fig. 6(b) to Fig. 7(b) occurred as the low-frequency limit of the filter was set from 3 μm^{-1} to 7 μm^{-1}. For the low-frequency limit larger than 7 μm^{-1}, the spatial features of the images remain roughly unchanged from those in Fig. 7(b). This result indicates that the transition from far-field dominant spatial characteristics to near-field dominant ones occurs in the spatial frequency range from 3 μm^{-1} to 7 μm^{-1}.

In Figs. 7(a) and 7(b), the electric (for the wire) and magnetic (for the void) field distributions both show periodic oscillations along the long-sides of the structures. Figures 7(c) and 7(d) show line profiles of the electric field for the nanowire and the magnetic field for the nanovoid, respectively, taken along the long side of the nanostructure. Peak positions (and as a consequence the period of the oscillation) for the nanowire nearly coincide with those of the nanovoid. From this point of view, the electric field distributions for the nanowire are consistent with the magnetic field distributions for the nanovoid for their high-frequency components. We also found from the analysis that the oscillating periods for both structures become long with increasing excitation wavelength in a consistent manner. These facts imply that Babinet's principle is compatible with the high spatial-frequency (or optical near-field) components of the electromagnetic fields near the metal screens in the visible to near-infrared spectral region.

The discussion described above, from the viewpoints of the spectral and spatial characteristics, suggests that Babinet's principle is applicable to high spatial-frequency (or near-field) optical fields for the complementary thin metallic screens, even if the prerequisite conditions, *i.e.,* infinitely thin and perfect-conducting screens, are not fully satisfied. The reason why the applicability of Babinet's principle is restricted to the high spatial frequency (or optical near-field) components has not yet become clear. Further experimental examinations with other substances and elaborated theoretical analysis including the near-field light source should be carried out to clarify the physical origins behind this observation.

4. Conclusion

We investigated the far-field and near-field spectroscopic properties of complementary nanostructured gold screens, nanowires and nanovoids using an aperture-type SNOM and discussed the applicability of Babinet's principle in the optical region. We found that Babinet's principle was not valid for the far-field transmission spectra of the complementary screens in the visible to near-infrared spectral region. The observed near-field transmission spectra showed only a slight resemblance between the complementary pair. We extracted the spectral features that are characteristic of near-field scattering by subtracting the far-field contribution from the near-field transmission spectra and found that the genuine near-field extinction spectra for the nanowire and nanovoid obtained in this way showed nearly complementary spectral features in accordance with Babinet's principle. We investigated near-field transmission images and simulated electromagnetic field distributions (with DDA method) for the complementary screens to examine the applicability of Babinet's principle from the viewpoint of the spatial characteristics. We found that the spatial features for the complementary screens showed little correlation to each other for both the near-field images and the simulated ones. On the other hand, we found from the Fourier analysis of the simulated images that the high spatial-frequency components of the electric field on the wire and those of the magnetic field on the void showed mutual spatial complementarity. The spectral and the spatial characteristics described above suggest that Babinet's principle is applicable to the high spatial-frequency (or optical near-field) components of electromagnetic fields for the complementary metal screens.

Funding